Sensors and Materials, Vol. 35, No. 12 (2023) 4459–4479
MYU Tokyo

S & M 3491

Investigation of a Discrete Model for Servo Feed Drive System in Machine Tool

Shean-Juinn Chiou,[1] Chun-Ting Chen,[2] and Ben-Fong Yu[3*]

[1]Department of Mechanical Engineering, National Chung Hsing University,
No. 145, Xingda Rd., South Dist., Taichung City 402202, Taiwan (R.O.C.)
[2]Intelligent Machinery Technology Center, Industrial Technology Research Institute,
No. 2, Wenxian Rd., Nantou City, Nantou County 540219, Taiwan (R.O.C.)
[3]Graduate Institute of Precision Manufacturing, National Chin-Yi University of Technology,
No. 57, Sec. 2, Zhongshan Rd., Taiping Dist., Taichung City 411030, Taiwan (R.O.C.)

(Received August 6, 2023; accepted December 6, 2023)

Keywords: mechatronic model, discrete model, system identification, PSO

In this study, we focus on creating a precise servo feed drive model to estimate the servo gains and the mechanical dynamics. Traditionally, manufacturers of machine tools rely on empirical methodologies to facilitate the development of new products. However, the emergence of Industry 4.0 prompted a shift towards virtual machine tool technology to assist product development management. The complete servo feed drive system comprises two integral components: the servo control system and the feed drive mechanism. In this study, we propose a discrete model for the servo control system to enhance the accuracy of the virtual digital model. when subjecting the real system to frequency sweep tests, particle swarm optimization (PSO) is employed to identify the parameters of the servo controller in the model. We observe tracking errors in the servo control system to validate the discrete model, and the predicted tracking errors closely match the experimental values, with the difference being within 2%. Furthermore, we consider external loads and couplings as the feed drive mechanism. We create a dual mass-spring-damping model to simulate the complete servo feed drive system. The digital model proposed in this paper can accurately predict the load inertia with an error of only 1.5% compared with the experimental values. In summary, we present a servo feed drive model for machine tools, enabling the estimation of external loads and couplings in a virtual environment. The advantages are reduced energy consumption, development time, and costs during product development.

1. Introduction

Most machine tool manufacturers traditionally develop new products on the basis of empirical methods and design new products through a process of trial and error, which is not only time-consuming but also costly. In recent years, with the emergence of Industry 4.0, technologies such as cyber physical systems and digital twins have found widespread application

*Corresponding author: e-mail: bfyu@ncut.edu.tw
https://doi.org/10.18494/SAM4704

ISSN 0914-4935
https://myukk.org/

in the machine tool industry. With this trend, numerous research studies on the development of virtual machine tool technology with the primary objective of reducing both the development time and associated costs of machine tools have been actively conducted. Beyond enabling the preproduction estimation of machine performance through simulation, these technologies also facilitate smart manufacturing simulation and the optimization of machining parameters. This study is dedicated to the development of virtual machine tool technology, including the establishment of accurate servo drive control models and the simulation of the machine's dynamic characteristics.

With the continuous improvement in computer processing power and escalating competition in the machine tool industry, the traditional approach of relying on empirical methods and trial and error for new product development has gradually transformed into leveraging computer simulation analysis to aid in design and development processes. Altintas *et al.*[1] proposed the concept of virtual machine tool (VMT) technology, wherein machines are modeled as digital models, facilitating predictive analysis of precision performance under such design scenarios through computer simulations. In instances where performance deviates from the expectation, immediate design modifications can be made, thereby conserving both the cost required for prototype manufacturing and the time expended on testing. The VMT technology lies in the precise establishment of digital models. When delving into discussions on machine tool dynamic accuracy, the servo feed system for each axis emerges as the primary source of influence. To accurately forecast machine performance, a reliable servo feed model is required.[2] Servo feed models must factor in various phenomena,[3] including the rigid body dynamics of the feed system,[4] friction within the feed system,[5–7] low-frequency resonance modes,[8,9] and the backlash of the feed drive mechanism.[10,11] Erkorkmaz and Wong[12] mentioned commonly employed servo loop models. These models can be broadly categorized into two control architectures. While these models account for friction phenomena in the feed system, they assume the current loop as 1. Matsubara *et al.*[13] established a servo loop model comprising current loops, velocity loops, and position loops. Sato[14] proposed a model composed of three layers of loops, considering phenomena such as friction, feed mechanism resonance, current saturation, and sensor resolution. Poignet *et al.*[15] considered the servo loop processing cycle and the lag stemming from signal sampling, by discretizing the continuous model and representing it in the z-domain. Regarding system identification, Saarakkala and Hinkkanen[16] employed PRBS signals as the excitation signals for identification experiments, which can broadly be categorized into three types: open-loop, direct closed-loop, and indirect closed-loop identification. The model parameters were determined using the input and output data acquired, employing the least squares method.[16,17] Erkorkmaz and Wong[12] provided a brief random NC code to induce rapid movements within a confined range for the test system, and the model parameters were determined using the least squares method after capturing the input and output. Subsequently, Wong and Erkorkmaz[18] employed the same excitation method but utilized a genetic algorithm for parameter identification, asserting that genetic algorithms expedite and enhance the accuracy of parameter identification. Chen *et al.*[19] sidestepped the nonlinear distortion of analog signals during analysis by utilizing square wave signals instead of traditional analog signal inputs. Ma *et al.*[20] divided the servo system into linear and nonlinear combinations during the identification process and established linear and nonlinear models separately. Two

distinct square wave signals were utilized as excitation sources, and the differential analysis of these signals was employed to estimate the system's linear model. The magnitude of dynamic friction was ascertained from experimental data collected during constant velocity segments.

In the majority of research endeavors, the establishment of continuous models is a common practice for servo feed systems. However, the continuous model represents an idealized model, assuming that controllers operate with infinitesimal time intervals. Actually, it is essential to acknowledge the practical constraints within real systems, where controllers necessitate finite computation time. Therefore, the primary objective of this study is to propose the development of a discrete model, thereby addressing these practical limitations and enabling the establishment of a robust servo control system.

The servo feed drive system presented in this paper is composed of a servo control system and a feed drive mechanism. In Sect. 2, we begin by deriving the servo loop model for the servo control system, encompassing both continuous and discrete models. The external load inertia is deduced as the feed drive mechanism, leading to the derivation of the dual mass-spring-damping model. The experimental method and system identification theory are introduced in Sect. 3. Section 4 presents the experimental results and discussion, including model validation, and estimation of external load and coupling parameters using the discrete model. Finally, a conclusion is provided in Sect. 5.

2. Cutting Principles and Experimental Setup

The servo feed drive system is a crucial component in machine tools, composed of a servo control loop and a feed drive mechanism. In high-speed machining, the impact of high acceleration and deceleration motion thrust on processing performance is more significant than that of cutting forces. In this section, we begin by deriving the model of the servo control system, which is divided into continuous and discrete models. Subsequently, the feed drive mechanism is simplified into a dual mass-spring-damping system, combining it with the servo control loop to establish a complete servo feed drive system.

2.1 Servo control system–continuous model

A typical servo control system comprises a multilayer closed loop, as illustrated in Fig. 1. The innermost current loop drives the actuator, and the plant generates a response in the velocity

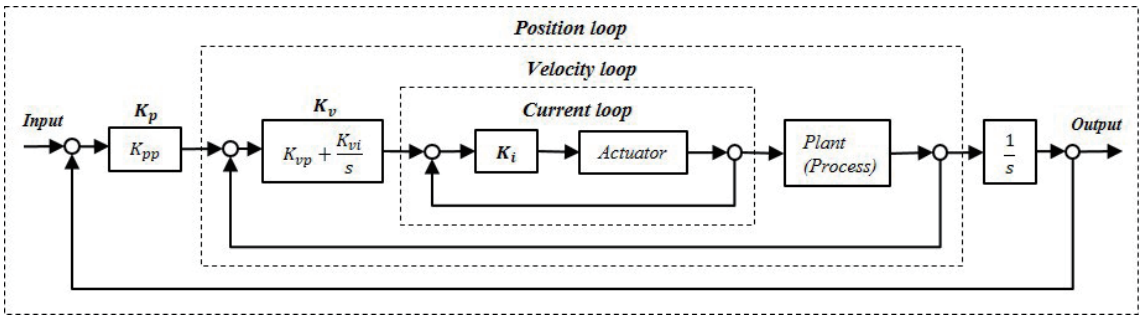

Fig. 1. Schematic diagram of experimental setup.

loop upon the instruction of the actuator. In this study, the plant is defined as the motor shaft mechanism. The outermost position loop is fed back by the position sensor. To guarantee system stability, the controller of each loop is suitably adjusted. The common controllers of the servo loop of the CNC machine tools mostly use a proportional (P)–integral (I) controller. In each loop, according to the difference between the input and output signals, the output signal is corrected by adjusting the PI controller so that the system responds accurately. A position loop controller (K_p) is usually a simple P controller, named position proportional gain (K_{pp}). A velocity loop controller (K_v) is a PI controller, named velocity proportional gain (K_{vp}) and velocity integral gain (K_{vi}). A commercial driver that allows the user to set the current loop controller (K_i) is not available. On the other hand, the current loop has a larger bandwidth than the other loops. Herein, the transfer function of the current loop (G_i) is set as a low-pass filter in this study.

$$G_i = \frac{1}{T_c s + 1} \tag{1}$$

Where, T_c is a time constant. When T_c becomes smaller, the system exhibits a higher bandwidth and a faster response.

Figure 2 shows the block diagram of the velocity loop that includes the current loop controller and motor model. The transfer function of the motor model (G_m) is

$$G_m = \frac{1}{J_m s + B_m}, \tag{2}$$

where the motor model includes the inertia moment (J_m) and viscous friction coefficient (B_m) of the shaft. The input of the current loop is the current command (i_c), and the output is the angular velocity of the motor (ω_m). Hence, i_c multiplied by G_i and torque constant (K_t) is the motor torque (T_m). T_m is applied to the motor shaft mechanism, and the motor shaft is rotated. ω_m is obtained through the motor shaft mechanism. The input of the velocity loop is the velocity command (ω_c). i_c is obtained after K_{vp} and K_{vi} of K_v are calculated, and ω_m is exported from G_m as the feedback signal of the velocity loop. Therefore, the transfer function of the velocity closed loop (G_v) is

$$G_v = \frac{\omega_m}{\omega_c} = \frac{K_v G_i K_t G_m}{1 + K_v K_i K_{tc} G_m}. \tag{3}$$

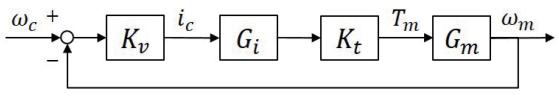

Fig. 2. Block diagram of velocity loop.

Figure 3 shows the block diagram of the position loop. The input is the position command (θ_c) after toolpath planning. Through K_{pp} of the position controller, ω_c is obtained for the velocity loop. The rotational angle of the motor ($\theta_m = \omega_m/s$) after the integration of ω_m is used as the input of the rotating transmission mechanism, where θ_m can be regarded as the displacement output of the motor shaft mechanism and is detected by the motor encoder. The transfer function of the position closed loop (G_p) is

$$G_p = \frac{\theta_m}{\theta_c} = \frac{K_{pp} G_v / s}{1 + K_{pp} G_v / s}. \tag{4}$$

2.2 Servo control system–discrete model

The continuous model derived in the previous section represents an idealized model, wherein the controller computes with infinitesimal time intervals and the sensor operates with an infinitely high sampling frequency. In actuality, controllers require finite computation time, and sensors have limited sampling rates. These limitations result in a delayed response of the system. Therefore, in this paper, we propose the development of a discrete model for establishing a servo control system. In this section, we shall discuss converting a continuous-time system into a discrete-time system.

Figure 4 is a typical discrete control system, where the input signal [$r(t)$] is processed through a digital controller, resulting in the output signals [$\hat{u}(t)$]. In the diagram, $G(z)$ represents the discrete controller, and "Clock" signifies the processing period of the discrete controller and the sampling period of the sensor. The analog-to-digital converter (A/D) and the discrete controller compute $r(k)$ from $r(t)$ as the output. The difference between $r(k)$ and $y(k)$ is then processed by a

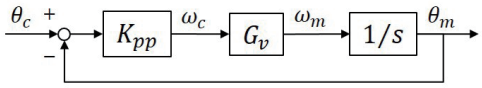

Fig. 3. Block diagram of position loop.

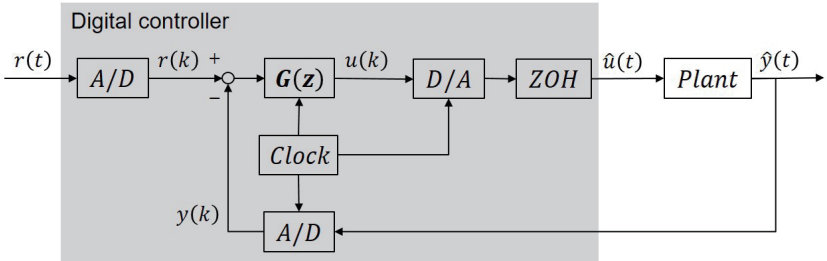

Fig. 4. A typical discrete control system.

digital-to-analog converter (D/A) and a zero-order hold (ZOH) to convert the discrete signal [$u(k)$] into a continuous signal [$\hat{u}(t)$]. $\hat{u}(t)$ is fed into the "Plant" to produce the response $\hat{y}(t)$, which is obtained through a sensor sampling process to yield $u(k)$. Since the plant is a continuous model, in this paper, we represent the process of obtaining $y(k)$ from the input $u(k)$ as an equivalent transfer function [$H(z)$], as illustrated in Fig. 5.

The control system can be discretized by various methods, such as the Tustin method, matched pole-zero method, and the forward Euler rule. In this study, the forward Euler rule is employed for discretizing the integrator, and the relationship between the s-domain and z-domain is expressed as

$$s = \frac{z-1}{T_s}, \tag{5}$$

where T_s represents the processing period of the controller. Next, the continuous model derived in the previous section is discretized. The discrete velocity loop model is derived in this section, and the transfer function of the discrete PI controller model [$K_v(z)$] is obtained as

$$K_v(z) = \frac{K_{vp}z + \left(T_s K_{vi} - K_{vp}\right)}{z-1}. \tag{6}$$

Owing to the significantly faster processing rate of the current loop compared with the velocity loop, it is assumed in this study that the current loop is a continuous system. Subsequently, by referring to the block diagram of the continuous velocity loop model in Fig. 2, the output of the velocity PI controller is discretized to obtain the discrete response of the motor's velocity. The result of discretizing the plant is

$$H(z) = \frac{K_t T_s^2}{z^2 + a_1 z + a_2}, \tag{7}$$

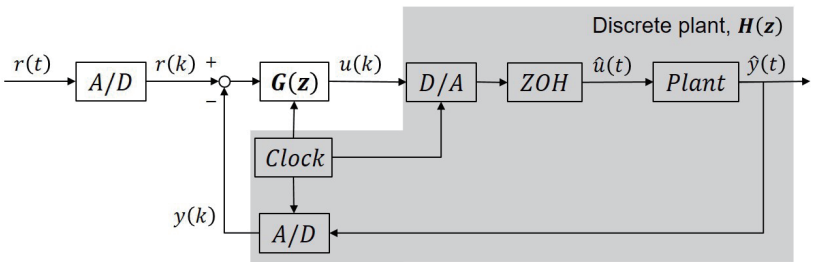

Fig. 5. Discretization of the continuous model of the plant.

where

$$a_1 = 2 + \frac{\left(J_m + b_m T_c\right) T_s}{J_m T_c},$$

$$a_2 = 1 + \frac{b_m T_s^2 - \left(J_m + b_m T_c\right) T_s}{J_m T_c}.$$

Figure 6 represents the block diagram of the discrete model of the velocity loop. The closed-loop transfer function from the input $\omega_c(z)$ to the output $\omega_m(z)$ is given by

$$G_v(z) = \frac{\omega_m(z)}{\omega_c(z)} = \frac{K_v(z) H(z)}{1 + K_v(z) H(z)}. \tag{8}$$

After substituting Eqs. (6) and (7) into Eq. (8), and the transfer function of the discrete velocity loop is

$$G_v(z) = \frac{\omega_m(z)}{\omega_c(z)} = \frac{K_t K_{vp} T_s^2 z + K_t T_s^2 \left(K_{vi} T_s - K_{vp}\right)}{z^3 + b_1 z^2 + b_2 z + b_3}, \tag{9}$$

where

$b_1 = a_1 - 1$,
$b_2 = K_t K_{vp} T_s^2 - a_1 + a_2$,
$b_3 = K_t T_s^2 \left(K_{vi} T_s - K_{vp}\right) - a_2$.

In this study, the processing period T_s serves as the processing period for both the velocity loop and the position loop. Position is calculated by accumulating velocity and feedback to the controller, as illustrated in Fig. 7. The closed-loop transfer function from the input $\theta_c(z)$ to the output $\theta_m(z)$ is

$$G_p(z) = \frac{\theta_m(z)}{\theta_c(z)} = \frac{K_{pp} G_v(z) \frac{T_s}{z-1}}{1 + K_{pp} G_v(z) \frac{T_s}{z-1}}. \tag{10}$$

After substituting Eq. (9) into Eq. (10), the transfer function of the discrete position loop becomes

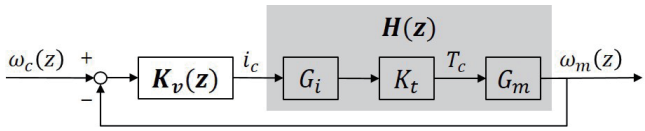

Fig. 6. Block diagram of discrete velocity loop.

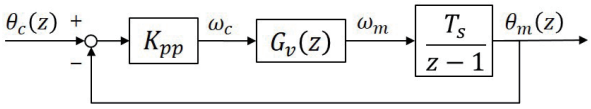

Fig. 7. Block diagram of discrete position loop.

$$G_p(z)=\frac{\theta_m(z)}{\theta_c(z)}=\frac{K_{pp}K_tK_{vp}T_s^3z+K_{pp}K_tT_s^3\left(K_{vi}T_s-K_{vp}\right)}{z^4+d_1z^3+d_2z^2+d_3z+d_4}, \tag{11}$$

where

$d_1=b_1-1$,
$d_2=b_2-b_1$,
$d_3=K_{pp}K_tK_{vp}T_s^3-b_2+b_3$,
$d_4=K_{pp}K_tT_s^3\left(K_{vi}T_s-K_{vp}\right)-b_3$.

2.3 Deduction of dual mass-spring-damping system

The feed drive mechanism is simplified into a dual mass-spring-damping system in this study. This system is useful for estimating the inertia moment (J_L) of the external loads outside the servo loop, as well as the stiffness (K_c) and damping (C_c) of the coupler. The motor torque T_m drives the rotation of the motor shaft with the inertia moment J_m, resulting in a rotational angle θ_m. Assuming a negligible rotational inertia moment of the coupling, T_m is transmitted through the coupling to drive the J_L of external loads, causing a rotational angle θ_L, as illustrated in Fig. 8.

According to Fig. 8, the equations of motion for the motor rotor and external load are

$$T_m-\left[K_c\left(\theta_m-\theta_L\right)+C_c\left(\dot{\theta}_m-\dot{\theta}_L\right)\right]=J_m\ddot{\theta}_m+B_m\dot{\theta}_m, \tag{12}$$

$$K_c\left(\theta_m-\theta_L\right)+C_c\left(\dot{\theta}_m-\dot{\theta}_L\right)=J_L\ddot{\theta}_L. \tag{13}$$

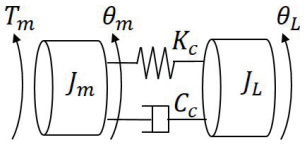

Fig. 8. Lumped model representation with the dual mass-spring-damping system.

We develop a block diagram of the dual mass-spring-damping system based on Eqs. (12) and (13), as illustrated in Fig. 9.

Owing to the feedback signals of the motor speed ω_m and motor rotational angle θ_m in the experimental platform, on the basis of the block diagram in Fig. 9 and Mason's gain formula, the transfer function from the motor torque T_m as input to the motor speed ω_m as output can be derived as

$$\frac{\omega_m}{T_m} = \frac{J_L s^2 + C_c s + K_c}{J_L J_m s^3 + (B_m + C_c) J_L s^2 + (C_c + K_c) B_m + (J_m + J_L) K_c}. \tag{14}$$

Combining the servo control system derived in the previous section with the dual mass-spring-damping model derived in this section allows for the further estimation of the parameters J_L, K_c, and C_c via the practical testing.

3. Experimental Method

3.1 Experimental setup

The experimental platform is a servo control system, as illustrated in Fig. 10. The control system adopts a commercial controller (0i-MF, Fanuc Corporation), and the process employs a servo motor and driver, which are also produced by Fanuc Corporation. The servo motor parameters K_t and J_m from Eq. (7) can be obtained from the motor specification sheet, where they are represented as 1.2 Nm/A and 0.0126 kgm^2, respectively. In this study, the experimental platform is developed for system identification, and a swept signal is used as the input. At the same time, the motor encoder is measured as the output. According to the frequency responses and the block diagram of the discrete model shown in Fig. 6, the system transfer function can be obtained by curve fitting. The parameters of the discrete model from Eqs. (6)–(11) are estimated by the system identification method.

To analyze the impact of external loads on the servo control system, we designed three types of load block, as illustrated in Fig. 11. The load inertia ratio represents the ratio of the load block's rotational inertia to the motor's inertia. In this study, the planned load inertia ratios for the external loads are 0.5, 1.0, and 1.5. The testing setup for the dual mass-spring-damping

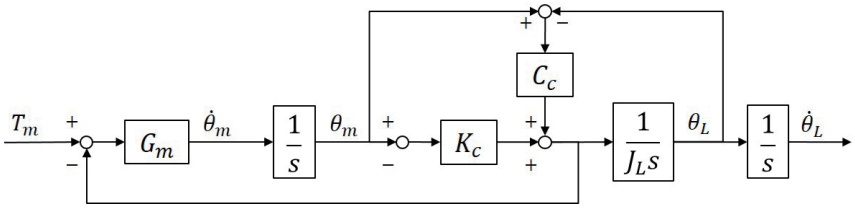

Fig. 9. Block diagram of dual mass-spring-damping system.

Fig. 10. (Color online) Experimental platform of servo-control system.

Fig. 11. (Color online) Three external load blocks for experiments.

system involves connecting the motor shaft to a coupling and then attaching the load block. To reduce the bearing load on the motor shaft, we designed an adjustable-height fixture to support the load block, as illustrated in Fig. 12. The coupling used in this setup is from ROTEX, the GS series, with the model number GS28-98-A-2.5.

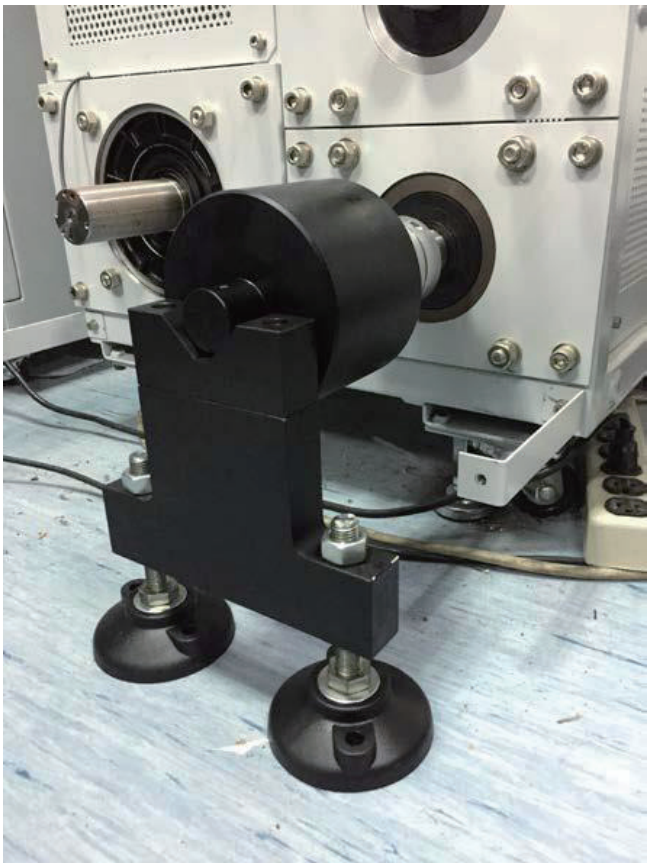

Fig. 12. (Color online) Experimental platform with the dual mass-spring-damping system.

3.2 System identification method

To estimate the unknown parameters of the discrete model, the servo control system is excited with an input signal, and the motor's output response data is measured. Particle swarm optimization (PSO) is then employed for curve fitting to determine the unknown parameter values.

PSO originated from the study of bird foraging behavior, where researchers observed that when one or a few birds find food, they would guide other birds in their direction. If each bird is treated as a particle, when one particle gets closer to the best solution, all particles tend to move in its direction, gradually converging towards the best solution. Since PSO not only considers information from the group but also uses its own information, it helps avoid getting stuck in local minima. Therefore, it is widely used in various optimization applications across different fields. To formalize this concept into mathematical equations, each particle has its current position and velocity. The best particle within the group is determined on the basis of the fitness function value. Then, each particle updates its flight velocity in accordance with its own inertia, individual experience, and group experience. The relationship between particle velocity and position updates can be expressed as

$$v_i(k+1) = Wv_i(k) + c_1 r_1 \left[p_i(k) - x_i(k) \right] + c_2 r_2 \left[p_g(k) - x_i(k) \right], \tag{15}$$

$$x_i(k+1) = x_i(k) + v_i(k+1), \tag{16}$$

where

$v_i(k + 1)$ is the velocity of particle i at time $k + 1$,
W is the inertia weight,
c_1 and c_2 are acceleration coefficients,
r_1 and r_2 are random values between 0 and 1,
$p_i(k)$ is the best position found by particle i up to time t,
$p_g(k)$ is the best position found by any particle in the group up to time t,
and $x_i(k + 1)$ is the position of particle i at time $k + 1$.

This update process is iteratively performed until convergence to find the optimal solution. The optimal solution defined in this study is the one where the root mean square error (*RMSE*) of the fitness function is minimized, which is expressed as

$$\text{Fitness Function} = \sqrt{\frac{\sum_{i=1}^{N} \left(\hat{y}_i - y_i \right)^2}{N}}, \tag{17}$$

where

y_i is the output from the actual system,
$\hat{y}_i$ is the output from the discrete model of the servo control system,
N is the number of samples, and
i is the i-th sample.

PSO is particularly useful for optimizing functions or models where traditional gradient-based methods may not be applicable.

4. Results and Discussion

The identification process of the servo control loop proceeds from the innermost loop, which is the current loop, followed by the velocity loop, and finally, the position loop. In this study, the current loop is simplified as a low-pass filter with only T_c requiring parameter estimation. Therefore, the current loop and velocity loop are identified together to obtain K_{vp}, K_{vi}, and T_c via the PSO method. Next, the identification process continues with the position loop to determine K_{pp}. Finally, external loads are introduced as part of the feed drive mechanism. In addition to identifying the load inertia and coupling stiffness, the effectiveness of the dual mass-spring-damping system is further validated.

4.1 System identification of velocity loop

The driver generates a sinusoidal waveform as an excitation signal, which is then used as the input. This signal is imported into the velocity command within the driver, and the output is obtained using the motor encoder. A mathematical model is constructed to represent the system's transfer function. Subsequently, PSO is employed to identify the unknown parameters (K_{vp}, K_{vi}, and T_c) in the discrete velocity loop's transfer function [Eq. (9)], with T_s set to 1 ms. Figure 13 shows the convergence of the fitness function values, showing that convergence is achieved after 60 iterations, with an *RMSE* of only 0.4462. Table 1 provides the actual values and the estimated parameter results. By substituting the identified parameters into Eq. (9), the system's transfer function can be expressed as

$$G_v(z) = \frac{\omega_m(z)}{\omega_c(z)} = \frac{3.322\times10^{-6}z - 2.951\times10^{-6}}{z^3 + 11.001z^2 - 20.996z + 8.995}. \tag{18}$$

Figure 14 shows the results of the experiment and simulation. The red line represents the experimental data, whereas the blue line represents the curve fitted using the PSO parameter estimation. The experimental results demonstrate that the discrete model adequately reproduces the system's response within a 500 Hz bandwidth. The errors between the experimental and estimated values for the parameters K_{vp} and K_{vi} are both within 4%.

4.2 System identification of position loop

When identifying the position loop, the parameters K_{vp} and K_{vi} of the velocity loop are kept unchanged. The position control in this study employs a simple proportional controller, denoted as K_{pp} in Fig. 7. Typically, the frequency range of interest for the position loop response is within 200 Hz, and a higher K_{pp} results in a wider bandwidth and reduced phase lag. Figure 15 illustrates the convergence of the fitness function, which occurs after 10 iterations, with an *RMSE* of only 0.0725. Table 2 presents the actual values and parameter estimates. Substituting the identified parameters into Eq. (11) yields the transfer function of the system as

$$G_p(z) = \frac{\theta_m(z)}{\theta_c(z)} = \frac{9.767\times10^{-8}z - 8.678\times10^{-8}}{z^4 + 10.001z^3 - 31.996z^2 + 29.991z - 8.995}. \tag{19}$$

Figure 16 depicts the results from experiments and simulations, where the red line represents experimental data, and the blue line represents the curve fitting results obtained through PSO parameter estimation. The experimental results demonstrate that the discrete model adequately captures the system's response within the 200 Hz range, with the error between the experimental and estimated values for K_{pp} being within 2%.

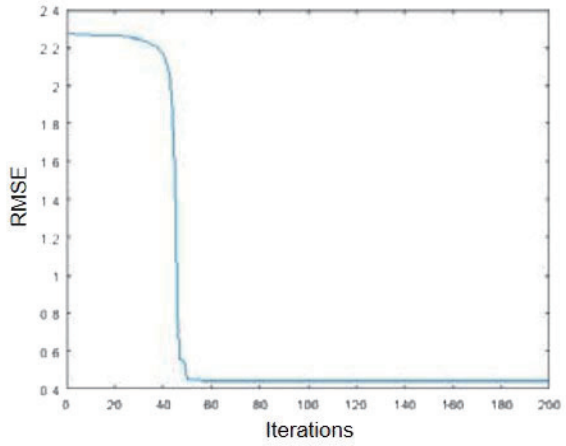

Fig. 13. (Color online) Convergence of fitness function in discrete model identification.

Table 1
Parameter estimation results for discrete velocity loop model.

	K_{vp}	K_{vi}	T_c
Actual	2.662	297.00	—
Estimation	2.768	308.57	0.0001

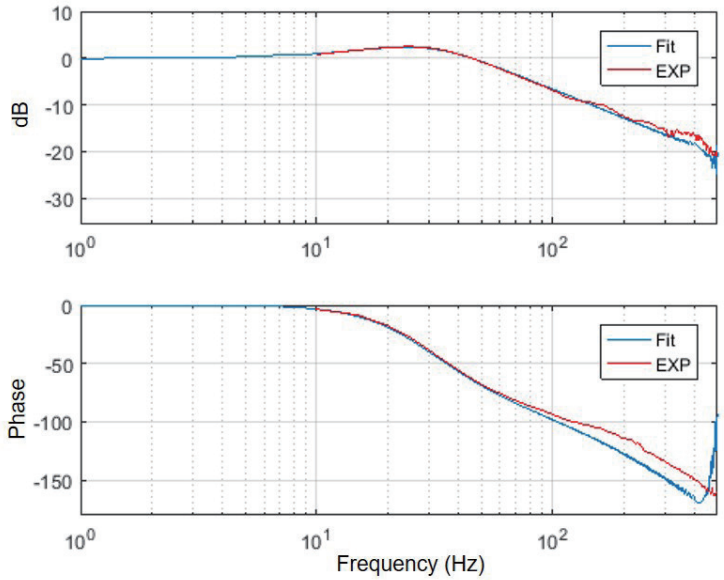

Fig. 14. (Color online) Experimental and simulation results for velocity loop.

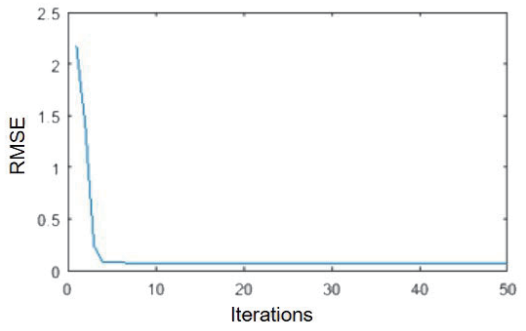

Fig. 15. (Color online) Convergence of fitness function in discrete model identification.

Table 2
Parameter estimation results for discrete position loop model.

	K_{pp}
Actual	30.000
Estimation	29.405

4.3 Validation of servo control system in time domain

The validation of the servo control system is performed through a back-and-forth motion with a 100 mm travel distance using G code. The error between the position command and the position feedback, known as tracking error, is observed. The test conditions involve the same K_{pp} but different feed rates, specifically, 3000 and 5000 mm/min. The results from both experiments and simulations are presented in Fig. 17, where the red line represents the experimental data, and the blue line represents the curve fitting results. The experimental results indicate that as the feed rate increases, the tracking error also increases. In Fig. 17(a), with a feed rate of 3000 mm/min, the tracking error during constant velocity segments is approximately 1.8%. In Fig. 17(b), with a feed rate of 5000 mm/min, the tracking error during constant velocity segments is approximately 2.0%.

Subsequently, the feed rate remains at 3000 mm/min, while the position proportional gains are varied to 30 and 50. Figure 18 illustrates the tracking error under these different conditions, where the red line represents experimental results, and the blue line represents the curve fitting results. The experimental data indicate that as the position proportional gain increases, the tracking error decreases. As shown in Fig. 18(a), with a position proportional gain of 30, the tracking error during the constant velocity segment is approximately 1.8%. In Fig. 18(b), with a position proportional gain of 50, the tracking error during the constant velocity segment is also approximately 2.0%.

The validation results indicate that the identified servo control model exhibits a time-domain tracking error of within 2% compared with experimental values, under various position gains and feed rates. Furthermore, this demonstrates that increasing the feed rate and position gain can effectively reduce tracking errors.

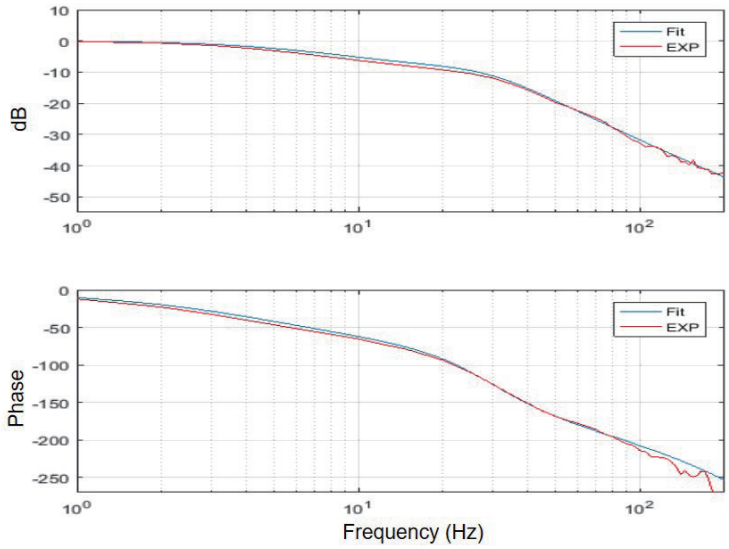

Fig. 16. (Color online) Experimental and simulation results for the position loop.

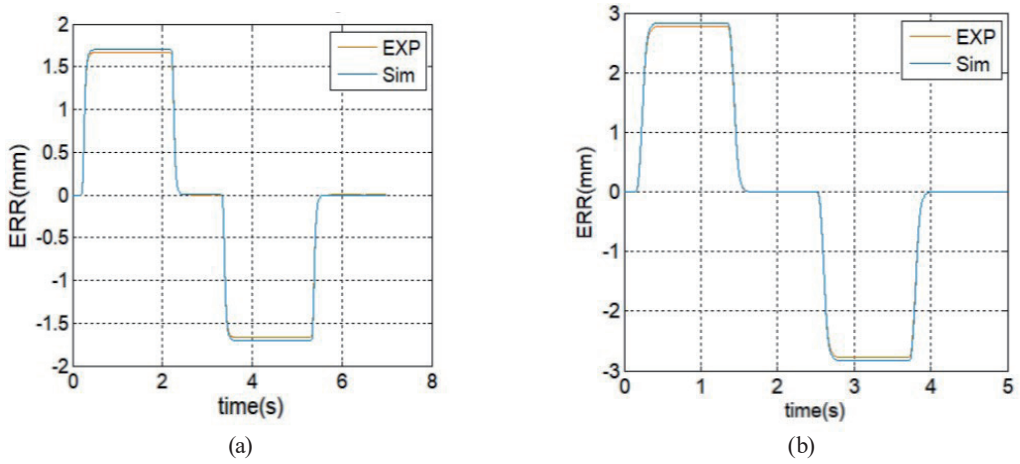

Fig. 17. (Color online) Tracking error analysis for different feed rates: (a) 3000 and (b) 5000 mm/min.

4.4 Testing of load inertia and coupling stiffness

Load inertia estimation is essential for constructing a comprehensive digital model of the servo feed drive system. In fact, load inertia estimation using a digital model in a virtual environment enables gain adjustments for the servo loop before actual machine setup. The complete servo feed drive system consists of both the servo control system and the feed drive mechanism. In this study, the controlled plant is simplified as a dual mass-spring-damping system. Additionally, we designed three inertia blocks to represent the feed drive mechanism.

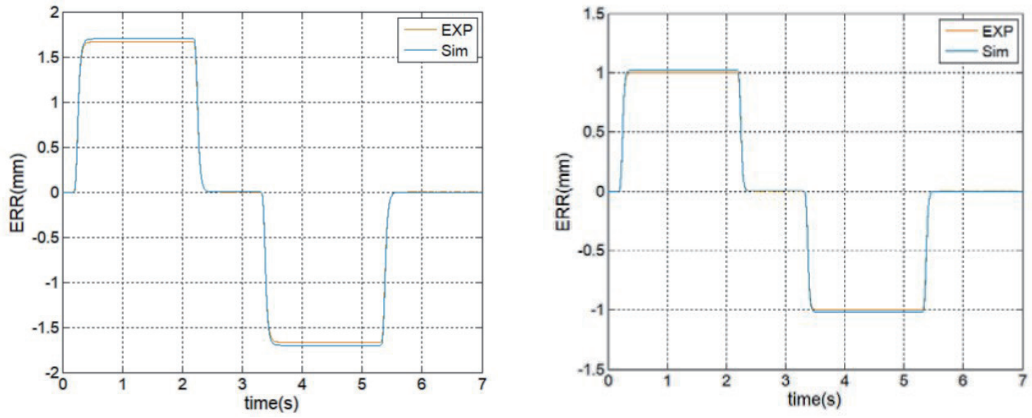

(a) (b)

Fig. 18. (Color online) Tracking error analysis for different position proportional gains. (a) Position proportional gain of 30 (b) Proportional gain of 50.

Figure 19 presents bode plots of the velocity loop for different load inertia ratios, specifically, 0.5, 1.0, and 1.5. From the experimental results, it is evident that as the load inertia ratio increases, the bandwidth of the velocity loop decreases.

First, experimental results with a load inertia ratio of 0.5 are utilized for parameter estimation using PSO, resulting in the determination of model parameters for the dual mass-spring-damping system, including the coupling stiffness K_c, coupling damping C_c, and external load J_L. These obtained model parameters are then substituted into Eq. (14), and the fitted curve is compared with the experimental results, as illustrated in Fig. 20. Table 3 presents the discrepancy between theoretical and estimated values for the load and coupling. The error between the designed and estimated values of external load is approximately 1.5%. The manufacturer's catalog provides a coupling stiffness value of 9920 Nm/rad, with an error of approximately 10.8% compared with the design and estimation values. However, there is no available design value for the coupling damping, and its estimated value through identification is 1.

Next, the coupling parameters K_c and C_c are set to 11000 and 1, respectively. The load inertia ratios of 1.0 and 1.5 are designed as inputs to the feed servo drive model. The velocity loop responses for different load inertia ratios are observed and compared with experimental results. Table 4 presents the results for designed and estimated load inertias. When the load inertia ratio is 1.0, the predicted load inertia is approximately 1.5% different from the design value. When the load inertia ratio is 1.5, the error in predicted load inertia compared with the design value is about 0.5%.

In this paper, we propose the establishment of a digital model for the complete servo feed drive system using the identification of experimental results with a load inertia ratio of 0.5. This identification process yields the parameters K_c and C_c of the coupling and provides an estimation of the load inertia. Subsequently, the estimated coupling parameters are incorporated into the model, and the model is validated with different load inertia ratios. The experimental results demonstrate that the digital model developed in this study can predict various load inertias accurately and also verify the correctness of the coupling parameters.

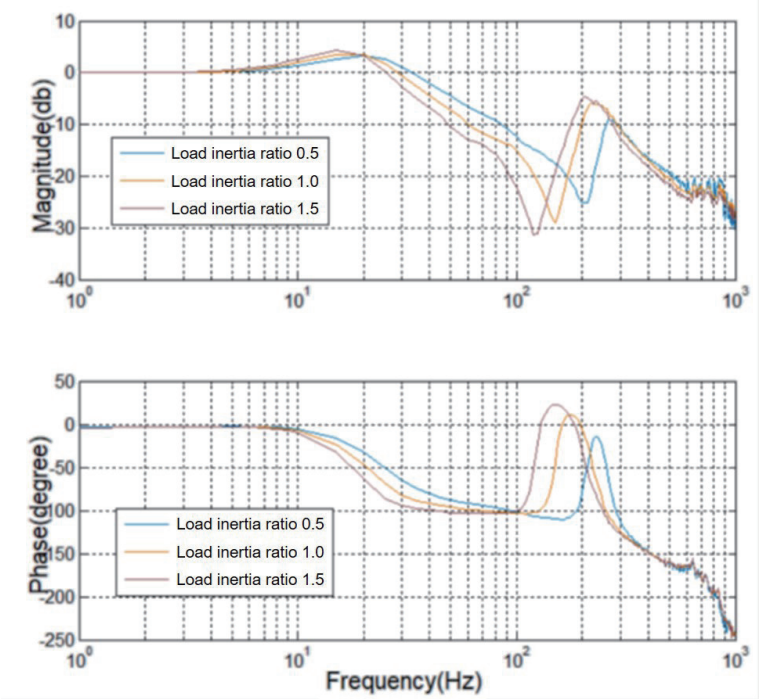

Fig. 19. (Color online) Velocity loop bode plots for different load inertia ratios.

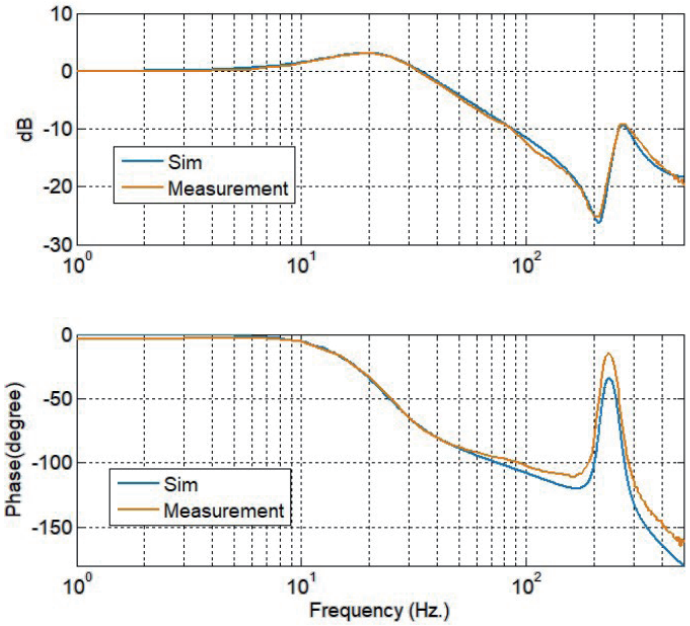

Fig. 20. (Color online) Experimental and simulation results for load inertia ratio of 0.5.

Table 3
Discrepancy between theoretical and estimated values.

	J_L	K_c	C_c
Theoretical value	6.3×10^{-4}	9920	—
Estimated value	6.4×10^{-4}	11000	1

Table 4
Theoretical and estimated load inertias for different load inertia ratios.

	load inertia ratio of 1.0	load inertia ratio of 1.5
Theoretical value	1.26×10^{-3}	1.89×10^{-3}
Estimated value	1.28×10^{-3}	1.90×10^{-3}

5. Conclusions

In machine tool development, manufacturers have been entrenched in time-consuming and empirical methods, characterized by iterative trial-and-error product development approaches. However, the emergence of Industry 4.0 has precipitated a shift within the machine tool development, leading to the widespread adoption of virtual machine tool technology while expediting product development, minimizing costs, and saving energy.

In this study, the digital model of the servo feed drive system for a machine tool, as well as a strategy to improve the modeling accuracy, was investigated. The work encompassed the construction of a servo control model that replicates an actual controller-driver-motor system and the assessment of external loads and couplings via a simplified dual mass-spring-damping model. The conclusions can be summarized as follows.

(1) Concerning the finite processing times and sensor sampling rates within practical servo control loops, in this study, we presented a more precise discrete model instead of the commonly used continuous model.
(2) The position loop controller and the velocity loop controller of the servo control model were identified by PSO.
(3) To validate the servo control model under various feed rates and position gains, we showed that this model has the capacity to reduce tracking errors effectively by elevating feed rates and position gains.
(4) The incorporation of a dual mass-spring-damping system completes the servo feed drive model. The experimental results demonstrated the model's precision in predicting various load inertias and validating the coupling parameters.

In this study, we proposed a digital model for the servo feed drive system, including the discrete model for the servo control system and the dual mass-spring-damping system for the feed drive mechanism. The proposed method will be applied to various types of machine tool with translation axes. In addition, the digital model will be investigated in order to analyze the behavior of translation axes.

Acknowledgments

This work was supported by the Ministry of Science and Technology, Taiwan (grant MOST 111-2222-E-167-001 – "Research on virtual mechatronic system and machining modes application based on tool center point of machine tools").

References

1 Y. Altintas, C. Brecher, M. Weck, and S. Witt: CIRP Ann. **54** (2005) 2. https://doi.org/10.1016/S0007-8506(07)60022-5
2 C.-H. Yeung, Y. Altintas, and K. Erkorkmaz: Int. J. Mach. Tools Manuf. **46** (2006) 10. https://doi.org/10.1016/j.ijmachtools.2005.08.002
3 K.-F. Lee and C.-H. Lee: Asian J. Control **22** (2020) 6. https://doi.org/10.1002/asjc.2292
4 Y. Koren: Computer Control of Manufacturing Systems (McGraw-Hill, New York, 1983).
5 B. Armstrong-Hélouvry, P. Dupont, and C. C. De Wit: Automatica **30** (1994) 7. https://doi.org/10.1016/0005-1098(94)90209-7
6 H. S. Lee and M. Tomizuka: IEEE Trans. Ind. Electron. **43** (1996) 1. https://doi.org/10.1109/41.481407
7 K. Erkorkmaz and Y. Altintas: Int. J. Mach. Tools Manuf. **41** (2001) 10. https://doi.org/10.1016/S0890-6955(01)00003-7
8 K. K. Varanasi and S. A. Nayfeh: J. Dyn. Sys. Meas. Control **126** (2004) 2. https://doi.org/10.1115/1.1771690
9 K. Erkorkmaz and A. Kamalzadeh: CIRP Ann. **55** (2006) 1. https://doi.org/10.1016/S0007-8506(07)60443-0
10 J. Y. Kao, Z. M. Yeh, Y. S. Tarng, and Y. S. Lin: Int. J. Mach. Tools Manuf. **36** (1996) 5. https://doi.org/10.1016/0890-6955(95)00064-X
11 J. F. Cuttino, T. A. Dow, and B. F. Knight: J. Mech. Des. **119** (1997) 1. https://doi.org/10.1115/1.2828782
12 K. Erkorkmaz and W. Wong: Int. J. Mach. Tools Manuf. **47** (2007) 9. https://doi.org/10.1016/j.ijmachtools.2006.08.025
13 A. Matsubara, Y. Kakino, and Y. Watanabe: Proc. 2000 Japan-USA Flexible Autom. Conf. (2000).
14 R. Sato: Key Eng. Mater. **516** (2012). https://doi.org/10.4028/www.scientific.net/KEM.516.154
15 P. Poignet, M. Gautier, and W. Khalil: 1999 IEEE/ASME Int. Conf. Adv. Intell. Mechatron. (1999). https://doi.org/10.1109/AIM.1999.803239
16 S. E. Saarakkala and M. Hinkkanen: IEEE Trans. Ind. Appl. **51** (2015) 5. https://doi.org/10.1109/TIA.2015.2416128
17 S. Villwock, A. Baumuller, M. Pacas, F.-R. Gotz, B. Liu, and V. Barinberg: 2008 34th Annu. Conf. IEEE Ind. Electron. (2008). https://doi.org/10.1109/IECON.2008.4758134
18 W. W. S. Wong and K. Erkorkmaz: Int. J. Adv. Manuf. Technol. **50** (2010) 275. https://doi.org/10.1007/s00170-009-2496-7
19 Y.-Y. Chen, P.-Y. Huang, and J.-Y. Yen: IEEE Trans. Control Syst. Technol. **10** (2002) 5. https://doi.org/10.1109/TCST.2002.801804
20 H. Ma, L. Wang, X. Su, and B. Shen: 2011 Int. Conf. Electr. Control Eng. (2011). https://doi.org/10.1109/ICECENG.2011.6057144

About the Authors

Shean-Juinn Chiou received his Ph.D. degree from University of Michigan, Ann Arbor, USA, in 1994. He has been an associate professor in the department of mechanical engineering, National Chung Hsing University since 1995. His research interests include mechanism design and analysis, CAE, design methodology, and engineering education.
(sjchiou@dragon.nchu.edu.tw)

Chun-Ting Chen received his B.S. and M.S. degrees from National Chung Hsing University, Taiwan, in 2015 and 2018, respectively. He has been working as an associate engineer at the Industrial Technology Research Institute since 2018. His research interests are in vibration, mechatronics, machining, and intelligent technology in machine tools. (GT.Chen@itri.org.tw)

Ben-Fong Yu received his B.S. and M.S. degrees from Da Yeh University and National Chung Cheng University, Taiwan, in 1999 and 2001, respectively, and his Ph.D. degree from National Chung Hsing University, Taiwan, in 2021. He worked in Goodway Machine Corp. and Ken Ichi Machine Co., Ltd., Taiwan, from 2002 to 2013 and 2017 to 2021, respectively. Since 2022, he has been an assistant professor at National Chin-Yi University of Technology. His research interests are in mechanical design, vibration, thermal issues, mechatronics, and intelligent technology in machine tools. (bfyu@ncut.edu.tw)